ROYAL SOCIETY OF CHEMISTRY

PAPER

Check for updates

Spray drying construction of hierarchical hollow ZnMn₂O₄ folded microspheres as anode materials for lithium ion batteries†

Yamin Zhang,‡ Senyang Xu,‡ Yuyan Wang, Linrui Hou [ID] * and Changzhou Yuan [ID] *

$ZnMn_2O_4$ (ZMO) has been paid close attention by researchers because of its high capacity of lithium storage, abundant reserves on earth, environmental friendliness and simple preparation process. However, as with most transition metal oxides, the low conductivity and the structural collapse caused by volume expansion limit the commercial application of ZMO. Herein, ZMO hollow folded microspheres (ZMO-HFs) are prepared by a spray-drying method. After annealing, ZMO-HFs with single and/or double shells are formed. The mixed shells not only increase the effective contact area between the electrolyte and active substance, but also shorten the Li^+ diffusion path and increase the active sites for the electrochemical reaction. In addition, the special structure can effectively alleviate the bulk expansion of the material to improve the cyclic rate performance of the material. Thanks to these attractive structural advantages, the obtained ZMO-HFs exhibit excellent rate behavior ($\sim$460 mA h g^{-1} at 2 A g^{-1}) and ultra-long cycle performance ($\sim$724 mA h g^{-1} after more than 400 cycles at 2 A g^{-1}). More importantly, this simple yet high-yield method will provide meaningful guidance for smart design/synthesis of other hollow materials.

1. Introduction

In 2000, Tarascon employed transition metal oxides as the anode for lithium ion batteries (LIBs) for the first time. Their high specific capacity enables them to be considered as an effective substitute for graphite-type anode materials.[1–4] Since then, transition metal oxides as a new class of anode materials have attracted attention from researchers. Among them, manganese transition metal oxides have rapidly attracted people's attention due to their environmental friendly nature, low cost, and abundant element reserves.[5–9] However, the electrochemical lithium storage performance is affected due to the large volume expansion and severe electrode powdering phenomena during charge and discharge. Therefore, in order to improve the defects of manganese oxides, researchers attempted to improve the volume expansion problem by combining with other metals, taking advantage of the synergy between the two metals. The results show that this method can effectively improve the electrochemical stability.[10–12]

Among these binary metal oxides, ZMO has attracted extensive attention from researchers due to its abundant element reserves on earth, low voltage platform, no pollution, low cost, and simple preparation method.[13–15] In addition, Zn and Mn elements in ZMO have different potential for lithium, so there will be a synergistic effect in the charge–discharge cycle. That is, when one metal reacts, another element acts as a buffer, reducing stress concentration problems during the Li^+ entrapment and stripping process and improving electrode powder phenomena.[16,17] Meanwhile, Zn in ZMO is alloyed with Li^+ to form ZnLi alloys, providing additional capacity. Accordingly, the theoretical ratio of ZMO is higher than that of other metal oxides.[18] Taken together, ZMO has unique advantages and is a strong contender for the next generation of anode material for LIBs.

Although ZMO has many advantages, the electrode pulverization issue occurs easily because of the large volume change in the process of Li^+ de-intercalation, which greatly restricts the application of ZMO in LIBs. Typically, the hierarchical structure design can provide a buffer space for volume expansion and prevent the structure from collapsing. Thus, the structural stability of electrode materials can be improved in the consecutive charge–discharge process.[19,20] In addition, the hollow structure can also effectively alleviate the stress concentration caused by the charging and discharging processes of the electrode material.[21,22] Zhang and colleagues[21] successfully

School of Materials Science & Engineering, University of Jinan, Jinan, 250022, P. R. China. E-mail: mse_houlr@ujn.edu.cn, mse_yuancz@ujn.edu.cn, ayuancz@163.com

† Electronic supplementary information (ESI) available. See DOI: https://doi.org/10.1039/d2ma00924b

‡ These authors contributed equally to this work.

synthesized layered porous ZMO microspheres by a simple ultrasonic spray pyrolysis technique combined with thermal annealing in air. This unique structure can not only facilitate the transfer of ions and electrons, but also adapt to large volume expansion and contraction. When used as a cathode material for LIBs, the discharge capacity is 1044 mA h g^{-1} after 300 cycles at a current density of 500 mA g^{-1}, and it has a high multiplier capacity (859 mA h g^{-1} at 2000 m A g^{-1}). Zhou et al.[23] prepared porous hollow rod-like ZMO HFs by a simple co-precipitation and annealing process. The electrochemical study of the anode material for laboratory use has shown that the material performs well in the current frequency range of 0.1–5 C, with a high reversible capacity of 902 mA h g^{-1} at 0.5 C after 320 cycles, especially 223 mA h g^{-1} at 5 C. This significant improvement in its electrochemical performance is mainly due to the synergistic effect of porous hollow structures and nanostructures. Therefore, the design of the hollow structure is of great value for employing ZMO.[24,25] Nonetheless, the preparation of hollow structures is complicated and has low yield, and some templates are difficult to remove.[26–28] It is therefore imperative to explore a simple preparation method for mass production.

In this study, we employ a simple spray-drying method to rapidly synthesize ZMO-HFs. Specifically, zinc acetate dehydrate, manganese acetate tetrahydrate as a metal salt source, and citric acid monohydrate as an organic ligand were employed. The unique single and double shell structure not only alleviates the volume expansion of ZMO, but also improves the specific surface area (SSA) and ionic mobility, giving it a long cycle life and excellent rate capability. As a result, the obtained ZMO-HF anode manifests excellent lithium storage properties with high-rate capabilities of $\sim$650 mA h g^{-1} at 0.1 A g^{-1}, and $\sim$460 mA h g^{-1} at 2 A g^{-1}, and superb cyclability of $\sim$724 mA h g^{-1} after 400 cycles at 2 A g^{-1}. This holds promise for its commercial application as an anode material for high-performance LIBs.

2. Experimental method

2.1 Reagents and materials

Citric acid monohydrate ($C_6H_8O_7 \cdot H_2O$), zinc acetate dehydrate ($Zn(CH_3COO)_2 \cdot 2H_2O$) and manganese acetate tetrahydrate ($Mn(CH_3COO)_2 \cdot 4H_2O$) were of analytical grade, and purchased from Sinopharm Chemical Reagent Co., Ltd. Acetylene black (AB), and carboxymethyl cellulose sodium (CMC) were purchased from Hefei Kojing Material Technology Co., Ltd.

2.2 Preparation of ZMO-HFs

First, 2.1285 g of $C_6H_8O_7 \cdot H_2O$ was added to 100 mL of deionized water. After being completely dissolved, 0.6585 g of $Zn(CH_3COO)_2 \cdot 2H_2O$ and 1.4706 g of $Mn(CH_3COO)_2 \cdot 4H_2O$ were added to the solution and stirred until completely dissolved. Then, the inlet temperature was set to 200 °C, the speed of the peristaltic pump was set to 25%, and the gas flow gauge was adjusted to 40 mm (600 L h^{-1}) before spray drying. The

precursor obtained after spraying was denoted as ZM-HFS-P, and further dried at 60 °C for 6 h to remove residual moisture. Finally, the precursor samples were placed in a muffle furnace and held for 2 h at 400 °C at a heating rate of 1 °C min^{-1}. After being cooled naturally, brown powder was obtained, and denoted as ZMO-HFs. For comparison, citric acid monohydrate was not used in the experimental process, and other conditions remained unchanged. The precursor sample after spray drying was named ZM-P, and the gray-black powder sample obtained after holding at 400 °C for 2 h was named ZZMO.

2.3 Materials characterization

The crystal phases of samples were investigated by X-ray diffraction (XRD, Rigaku Ultima IV) with a 2θ range from 10 to 80°, a scanning speed of 10° min^{-1}, and a test voltage of 40 kV. X-Ray photoelectron spectroscopy (XPS, Thermo ESCA-LAB 250Xi) was used to determine the elemental species and chemical composition on the surface of the sample. The micromorphology and structure of the samples were observed by field-emission scanning electron microscopy (FESEM) and transmission electron microscopy (TEM) (JEOL JEM 2100 system). Thermo-gravimetric analysis (TGA) data during the heating process were obtained using a DTG-60H TGA analyzer of Shimadzu Company, Japan (from 30 to 600 °C). The SSA and pore structure information were collected using an Autosorb-IQ of Canta Instrument Company, USA.

2.4 Electrochemical evaluation

To prepare the working electrode, the as-prepared ZMO-HFs (70 wt%), AB (20 wt%), and CMC (10 wt%) were dissolved in deionized water to form a homogenous and particle-free slurry after being fully ground. The slurry was coated on copper foil, and dried in a vacuum oven at 110 °C for 12 h to remove moisture thoroughly. Circular negative electrodes of 12 mm diameter were cut using a punch. The CR2032 battery case was selected and assembled in an argon atmosphere glove box following the assembly sequence of negative, diaphragm, lithium sheet, gasket and shrapnel (high pure argon environment, water/oxygen content <0.1 ppm). An appropriate amount of electrolyte (1 M LiPF$_6$, EC: DMC: EMC = 1: 1: 1 in volume) was added during the assembly process, and the assembled battery was left to stand for 12 h. Galvanostatic charge and discharge (GCD) tests were carried out with a Land CT2001A battery test system. The cyclic voltammetry (CV) and electrochemical impedance spectroscopy (EIS) tests were conducted on an electrochemical workstation (IVIUM, the Netherlands).

3. Results and discussion

3.1 Physical characterization of ZMO-HFs

The synthetic process of the porous hollow folded microspheres is illustrated in Scheme 1. First, citric acid monohydrate is dissolved in deionized water. Then the metal salt is added to the solution, spray dried into a white powder, and after further annealing, ZMO-HFs were obtained. The microspheres formed
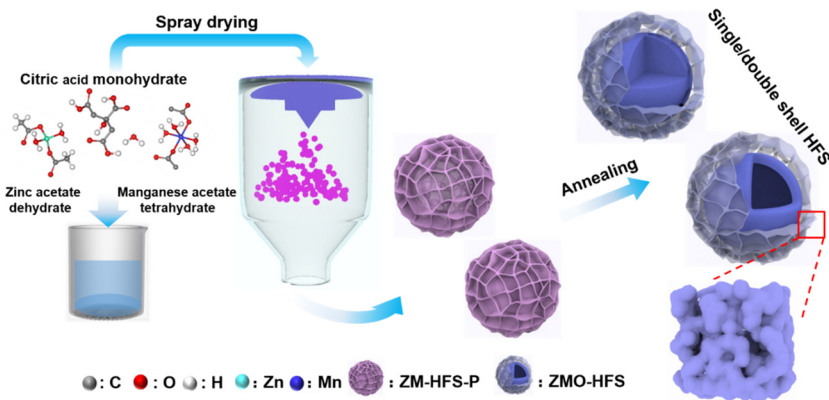
Scheme 1 Schematic illustration of the synthesis process of the ZMO-HFs.

by spray drying have weak intermolecular binding forces, and some materials need to be added to prevent structural collapse during heat treatment. As a metal ion complexant, citric acid monohydrate can be well complexed with Zn^{2+} and Mn^{2+} ions. At the same time, citric acid, as an organic substance, can be used as a carbon source to stabilize the microstructure of the sample and prevent structural collapse due to stress shifts in the sample during heat treatment.

To understand the microstructure of the spray-dried precursor sample, FESEM and TEM were used to characterize the ZM-HFS-P sample, as shown in Fig. 1. The samples obtained after spray drying are spheres with wrinkled surfaces and different sizes (1–10 μm) (Fig. 1a). It can be observed that the sample surface is relatively smooth when a sphere is enlarged (Fig. 1b). TEM tests were used to observe the internal microscopic morphology to explore more about the internal conditions of the microspheres. As can be seen from Fig. 1c and d, some microspheres have solid structures, while some samples have cavities inside. The cavity formation of the precursor is ascribed to the rapid volatilization of the liquid, as part of the droplet passes through the elevated temperature region of the nozzle, which causes the volume of the microspheres to expand to form an internal cavity structure.[29] ZMO was formed from the precursor sample after heat treatment at 400 °C for 2 h. The XRD pattern, as shown in Fig. 2a, corresponds perfectly to the PDF standard card of JCPDS No. 71-2499, confirming the pure phase ZMO with a tetragonal spinel structure formed after annealing.

In order to explore the formation process of ZMO-HFs during annealing, we conducted TGA tests on ZMO-HFs-P in
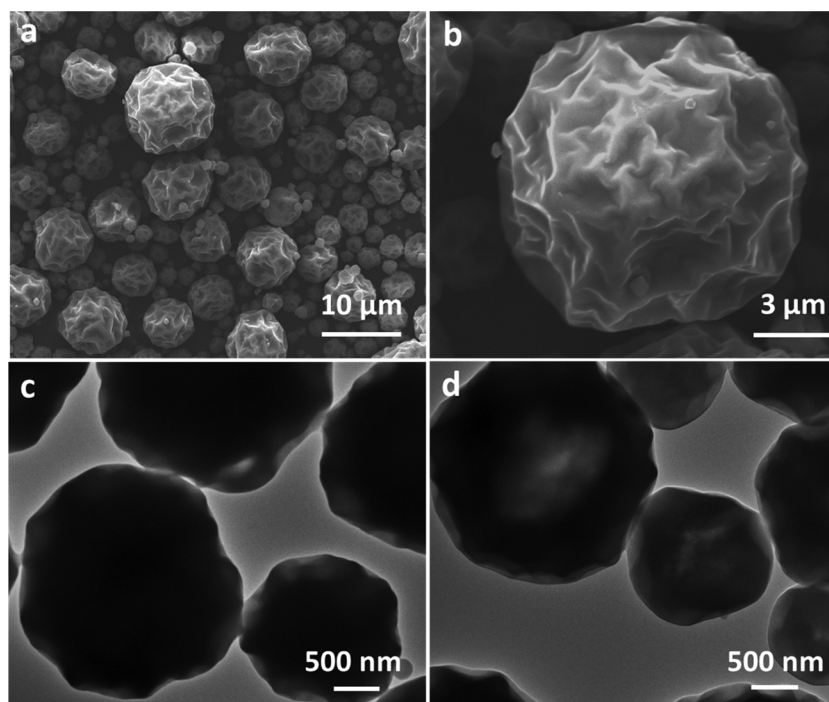

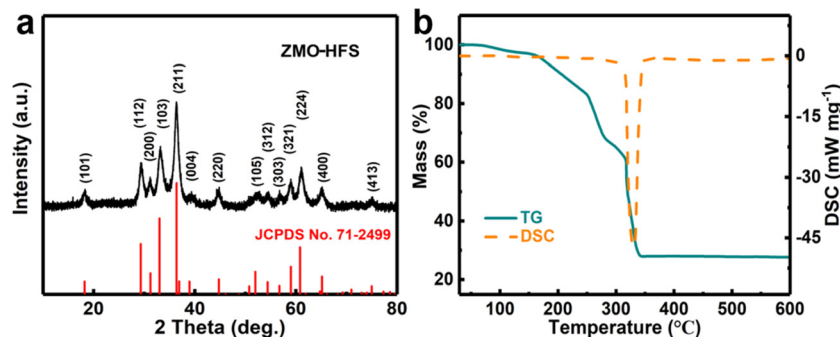**Fig. 1** (a and b) FESEM and (c and d) TEM images of the ZM-HFs-P.

Fig. 2 (a) XRD images of the ZMO-HFs. (b) The TG-DSC curve of the ZM-HFs-P under oxygen conditions.

air. The corresponding TGA data of the ZM-HFS-P precursor in the air are shown in Fig. 2b. As can be seen from the diagram, the mass of the TGA curve decreased slowly before 160 °C, indicating that the mass loss in this temperature range mainly results from the water absorbed in the precursor sample. The accelerated mass loss between 160 and 310 °C, equivalent to organic/inorganic decomposition, can be observed as the temperatures increase. The sample mass decreased rapidly between 310 and 340 °C, and the corresponding DSC curve shows an exothermic reaction, partly attributed to the further oxidation of metal salt ions to ZMO. At 340 °C, there is no significant loss of sample mass, indicating that the metal salt in the sample is oxidized into stable ZMO, without the occurrence of any other reaction.

In order to obtain further a detailed element composition and valence state information of ZMO-HFs, XPS analysis was performed on ZMO-HFs. As shown in Fig. 3a, the presence of Zn, Mn, and O elements in the sample is easily visible on the XPS full

spectrum scan of ZMO-HFs. Each element was then specifically analyzed by high-resolution XPS spectroscopy. As shown in Fig. 3b, the high-resolution spectrum of Zn 2p and the fitted curve, where 1021.2 eV and 1044.3 eV correspond to the 3/2 and 1/2 spin orbits of Zn 2p in the high binding energy state respectively. The difference in the spin levels between the two peaks is 23.1 eV, suggesting the existence of Zn^{2+} in the sample.[30–34] Mn 2p high-resolution spectroscopy and fitting curves (Fig. 3c) show that 641.8 eV and 653.5 eV correspond to the 2/3 and 1/2 spin orbits of Mn 2p, respectively, with an energy level difference of 11.7 eV between the two orbits, indicating the presence of Mn(III) in the sample.[30,31] The high-resolution spectra of O 1s (Fig. 3d) show the binding energy positions at 530.0 and 531.6 eV after fitting, which are attributed to the existence of two forms of oxygen elements in the sample. More specifically, the one at 530.0 eV corresponds to the metal (Zn/Mn) oxygen bonds, and the other at 531.6 eV is related to the water and/or surface hydroxyl groups in ZMO-HFs samples.[35,36]
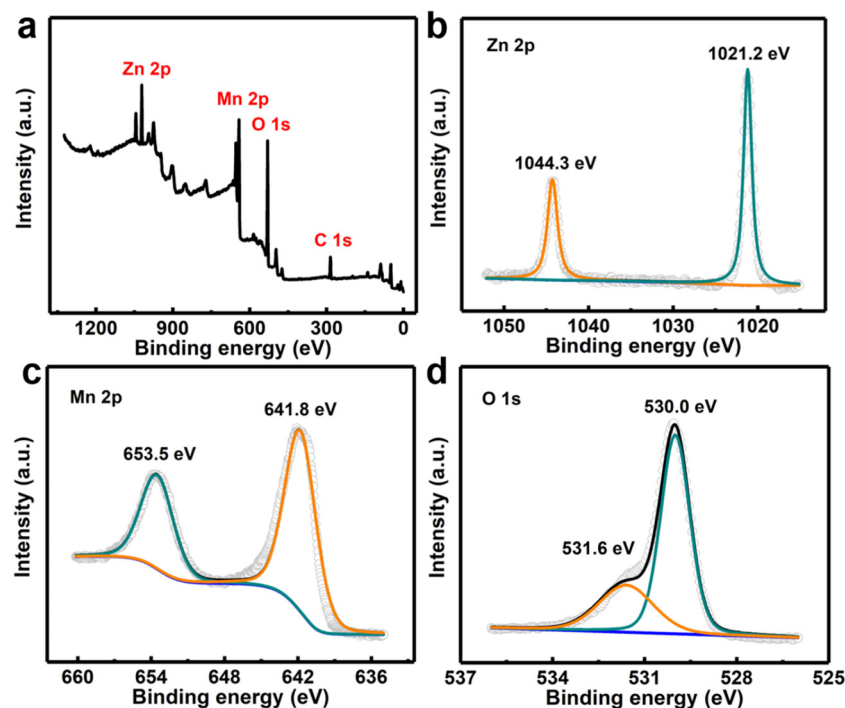

Fig. 3 (a) XPS full-spectrum scans and high-resolution elemental (b) Zn 2p, (c) Mn 2p, and (d) O 1s spectra of the ZMO-HFs.

From the microscopic morphology characterization of ZM-HFs-P, it is observed that the sample obtained after spray drying is a solid/hollow mixed folded microsphere with a smooth surface. To observe microscopic morphological changes of precursors after annealing, we tested and analyzed them using FESEM and TEM, as shown in Fig. 4. The microstructure of the sphere remains intact after heat treatment at 400 °C (Fig. 4a). After further magnification, more surface folds are evident, when compared to the precursor samples (Fig. 4b). According to the further characterization of the damaged sphere (Fig. 4c), it is found that the heat-treated sphere may be a double-shell hollow structure (the shell thickness is ∼437 nm). To verify the results of the FESEM test, the internal structure of the folded microsphere is again observed by TEM. As shown in Fig. 4d, there is a single-shell hollow structure in the ZMO-HFs, while some of the samples are double-shell hollow structures as observed from Fig. 4e, and the thickness is similar to those in Fig. 4c. The appearance of the single/double shell hollow microspheres is due to the rapid volatilization of the solvent during the process of the droplets being ejected through the nozzle, causing the metal ions to diffuse outward. Meanwhile, the non-uniformity of the nozzle temperature leads to different volatilization rates of the liquid in different droplets, so that the degree of diffusion of metal ions to the outside is different. Fig. 4f shows that the ZMO-HFs are composed of many nanoparticles. There are abundant pore structures between the particles, which increase the effective contact area between the active material and the electrolyte, and greatly enhance the reactive sites, to improve the electrochemical lithium storage performance of the electrode material. Besides, the high-resolution TEM (HRTEM) images (Fig. 4g) show that the measured lattice spacing of the two amplified regions is 0.48 nm and 0.28 nm, respectively, corresponding to the (101) and (200) crystal planes. A clear polycrystalline diffraction ring can be observed from the SAED diagram, which proves that it has a polycrystalline structure and corresponds to the (211), (112), and (220) crystal planes in ZMO. The STEM image (Fig. 4h) and the corresponding EDS elemental mapping map show that Zn, Mn and O elements are evenly distributed in ZMO-HFs.

In order to explore the factors affecting the micromorphology of ZMO-HFs, the microspheres obtained from spray-dried salt solutions without the addition of citric acid monohydrate were compared and FESEM tests were performed. Most of the ZM-P samples are spheres with a folded surface (Fig. S1a, ESI†), but the sphere surface is not as folded as those of ZM-HFs-P and the surface is smooth (Fig. S1b, ESI†). After heat treatment, the microstructure of ZM-P was completely destroyed under the same heat treatment conditions (400 °C, 2 h), revealing a microscopic particle condensation state (Fig. S1c and d, ESI†). The results indicate that citric acid monohydrate, a complexing agent of metal ions, easily combines with Zn^{2+} and Mn^{2+} ions, enhancing the intermolecular binding ability. Meanwhile, citric
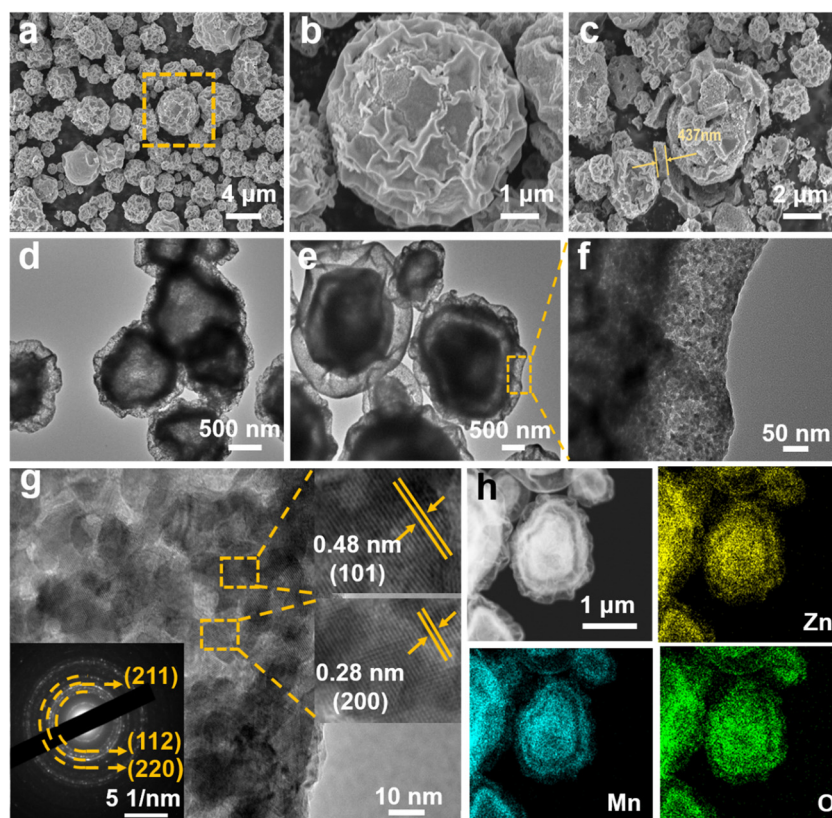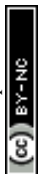

Fig. 4 (a–c) FESEM images, (d–f) TEM images, (f) HRTEM image (illustration: SAED image), (h) STEM and the corresponding EDS elemental mapping images of the ZMO-HFs.

acid as an organic matter provides a stable carbon framework for the sphere, effectively alleviating the stress concentration phenomenon caused by the heating process. At the same time, to explore the influence of citric acid monohydrate on the phase composition of the sample, we conducted XRD tests on ZZMO (Fig. S2, ESI†). The XRD pattern of ZMO can be observed corresponding to the PDF standard cards JCPDS No. 71-2499 and JCPDS No. 89-0510, corresponding to $ZnMn_2O_4$ and ZnO, respectively, further illustrating the importance of citric acid monohydrate for ZMO-HF formation.

TEM tests have revealed that ZMO-HFs are composed of a large number of nanoparticles and that the pore structure also affects their electrochemical properties. Therefore, a BET analysis was performed on ZMO-HFs to thoroughly explore their pore properties. As can be seen from the N_2 adsorption–desportion curve diagram (Fig. S3a, ESI†), ZMO-HFs have a typical IV curve. The hysteresis loop in the 0.5–1 range indicates that ZMO-HFs have obvious mesoporous characteristics. As can be seen from the pore size distribution curves (Fig. S3b, ESI†), the pore sizes are mainly distributed in the 3–30 nm range, which further proves that ZMO-HFs are mesoporous structures. The results show that the SSA of porous ZMO-HFs is $\sim$89.8 m^2 g^{-1}, the average pore size is $\sim$10.0 nm, and the pore volume is 0.22 cm^3 g^{-1}. The abundant pore structure significantly enhances the electroactive sites of electrode

materials and improves the ion transport rate. The porous hollow structure effectively alleviates the volume change during charging and discharging. It significantly improves the transport of ions/electrons inside the electrode material, providing a basis for its excellent electrochemical properties.

3.2 Electrochemical characterization of ZMO-HFs

Based on the above phase test and analysis results, the ZMO-HFs are highly expected to exhibit superior Li-storage properties. Fig. 5a displays the CV curves of the ZMO-HFs for the 1st, 3rd and 5th cycles tested at 0.5 A g^{-1}. In the scan of the 1st cycle, the appearance of a weak reduction peak at 1.18 V indicates that the irreversible lithiation of Li^+ occurred during the discharge process of the 1st cycle. In addition, a sharp reduction peak appeared at 0.25 V during the formation of elemental metals Zn and Mn. The peak below 0.25 V corresponds to the alloying reaction of ZnLi.[37,38] During the oxidation reaction, the oxidation peaks at 1.25 and 1.63 V overshoot, indicating that Zn^{2+} and Mn^{2+} are oxidized to ZnO and MnO, respectively.[39,40] In the 3rd cycle, the corresponding reduction peaks for Zn^{2+} and Mn^{2+} are at 0.61 V and 0.40 V, respectively, which are the same as in the first oxidation process. The oxidation peaks at 1.25 and 1.63 V indicate the oxidation of metallic Zn/Mn to generate ZnO/MnO. The redox reaction shown in the 5th cycle
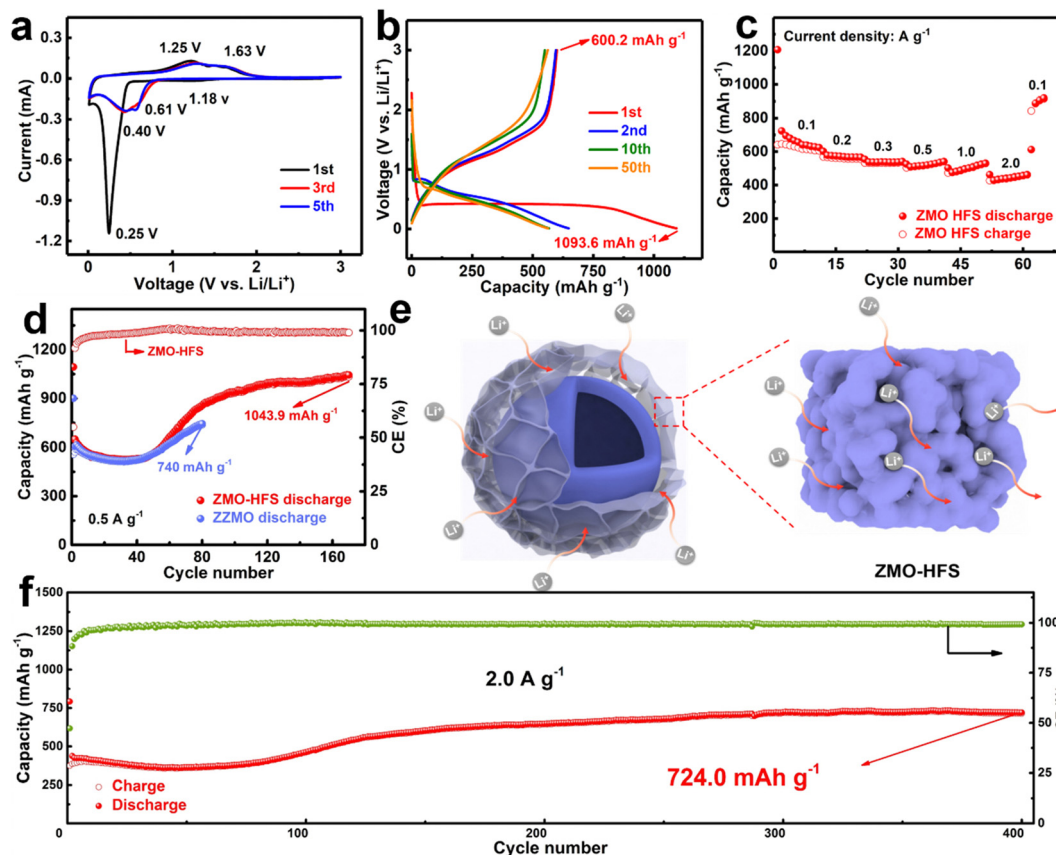

Fig. 5 (a) CV curves, (b) charge–discharge curves at 0.5 A g^{-1}, (c) rate performance at a current density of 0.1–2.0 A g^{-1} of the ZMO-HF electrode. (d) Comparative cycling performance of the ZMO-HFs and ZZMO electrodes at a current density of 0.5 A g^{-1}.

is essentially the same as that in the 3rd cycle, indicating the excellent electrochemical reversibility.

At a current density of 0.5 A g^{-1}, the discharge specific capacity of ZMO-HFs in the first cycle reaches 1093.6 mA h g^{-1} (Fig. 5b), along with a charge specific capacity of 600.2 mA h g^{-1}, corresponding to an initial CE of 54.9%, which is higher than that of ZZMO ($\sim$43.0%, Fig. S4a, ESI†). In addition, the greater decrease in capacity is primarily due to the decomposition of the electrolyte and the formation of the SEI film. The charge and discharge specific capacities were 595.3 mA h g^{-1} and 648.5 mA h g^{-1} during the second cycle, and the CE increased to 91.8%. In the subsequent 10th and 50th laps of the tests, the CE values are up to 96.9% and 99.9%, respectively. The improvement of CE indicates that the electrode material has excellent electrochemical reversibility.

The rate capability was then investigated in view of the unique porous hollow structure of ZMO-HFs. As depicted in Fig. 5c, the ZMO-HFs show excellent rate behavior with large discharge capacities of $\sim$658.7, $\sim$522.7, $\sim$501.8 and $\sim$445.7 mA h g^{-1} at current densities of 0.1, 0.2, 0.3, 0.5, 1.0, and 2.0 A g^{-1}. When the current density returned to 0.1 A g^{-1}, the discharge specific capacity could reach 886.5 mA h g^{-1} again. Therefore, the hollow structure can effectively alleviate the electrode powder problem caused by Li$^+$ insertion/extraction at different current densities. Fig. 5d shows the cycle stability test at a current density of 0.5 A g^{-1}. In the first 40 cycles, the decayed charge/discharge capacities of the ZMO-HF electrode material are mainly due to the formation of the SEI film and the decomposition of the electrolyte during cycling. Afterward, the charge/discharge specific capacity of the electrode material increased slowly, mainly because the nanoscale pristine ZMO particles would evolve into smaller ZnO and MnO particles upon cycling, which would shorten the Li$^+$ diffusion pathway. Meanwhile, some inactive metals Zn and Mn accumulate in the electrode and improve the electronic conductivity, and the continuous activation process of the material leads to the increase of the capacity.[41] The material capacity reaches a stable state near the 120th cycle. After the 160th cycle, the discharge specific capacity of the electrode material is 1043.9 mA h g^{-1}, which is superior to that of the ZZMO ($\sim$740 mA h g^{-1} after the 80th cycle) without citric acid monohydrate addition (Fig. 5d). Evidently, the addition of citric acid monohydrate helps to maintain the structural integrity of ZMO-HFs, which is an important basis for their excellent electrochemical performance. In addition, EIS was performed on newly assembled half-cells to test and analyze the dynamical behavior of the ZMO-HF electrode material (Fig. S4b, ESI†). Evidently, the impedance plot is mainly composed of a semicircle (middle and high frequency regions) and a tilted straight line in the low frequency region. The diameter of the semicircle in the high-frequency region represents the charge transfer resistance (R_{ct}), which usually reveals the resistance of electrochemical reactions at the electrode–electrolyte interface. The higher the slope of straight line in the low-frequency region is, the higher the diffusion coefficient of Li$^+$ is. The R_{ct} value is calculated to be 167.2 Ω for the ZMO-HF electrode, highly favoring efficient lithium storage. Therefore, the porous hollow

structure not only brings a larger contact area between active substances and the electrolyte, but also speeds up the transmission speed of Li$^+$. Furthermore, in order to test the application value of ZMO-HFs under the conditions of rapid charge/discharge of LIBs, we performed uninterrupted cyclic charge/discharge tests at a current density of 2.0 A g^{-1} (Fig. 5f). After 400 cycles of high current charge/discharge cycles, the discharge-specific capacity of ZMO-HFs can be maintained at 724 mA h g^{-1}. The excellent electrochemical performance of ZMO-HFs is due to their special structural characteristics. That is, the porous hollow structure effectively alleviates the problem of electrode pulverization caused by the Li$^+$ intercalation/de-intercalation process. Meanwhile, the larger SSA can increase the contact area of the electrode material and the electrolyte, and increase the actual active sites for the electrochemical reaction.

In short, the ZMO-HF samples prepared with PHFs exhibit excellent Li$^+$ storage capacity (Fig. 5e), the reason for which can be concluded as follows: (I) the hollow structure can effectively alleviate the electrode chalking problem caused by the Li$^+$ embedding shedding process. (II) The folded surface of a material can increase its SSA. A high SSA can ensure sufficient contact between the electrolyte and the electrode surface. At the same time, the abundant micropores can be used as additional sites for the adsorption of capacitive Li$^+$, improving the reversible specific capacity. (III) Highly developed porous structures can provide sufficient and extensive Li$^+$ diffusion channels, thereby achieving fast and stable Li$^+$ diffusion.

Based on the above electrochemical performance tests, and to explore the underlying reasons for the excellent electrochemical lithium storage performance of ZMO-HFs, the CV method was used to analyze their kinetics. Fig. 6a shows the CV curve of the electrode material at a scan rate of 0.2 $^-$ 1.4 mV s^{-1}, where the relationship between the scan (ν) and peak current (i) can be expressed as:[42–44]

$$i = a\nu^b \tag{1}$$

$$\log i = b \log \nu + \log a \tag{2}$$

where a and b are adjustable values determined by fitting the $\log(\nu)$ vs. $\log(i)$ plots. When the peak current changes with the power of 0.5 of the scanning voltage, that is, the b value is equal to 0.5, then the storage behavior of the electrode is similar to that of a battery and is controlled by diffusion. When the peak current changes linearly with the scanning voltage, that is, b is equal to 1.0, the storage behavior of the electrode is similar to that of a capacitance and is controlled by the adsorption process. The calculated b values are presented in Fig. 6b. Clearly, in the scan rate range of 0.2–1.4 mV s^{-1}, b_a and b_c, corresponding to the oxidation and reduction peaks, respectively, are calculated as 0.70 and 0.78, indicating the pseudocapacitance-dominated Li-storage performance of the ZMO-HFs. In addition, when the voltage is constant, the total capacity contribution at different scan rates can be divided into two parts: $k_1\nu$ controlled by the surface pseudocapacitance behavior, and $k_2\nu^{1/2}$ controlled by the diffusion behavior. These two have the following relationship (k_1 and k_2 are constants):[44]
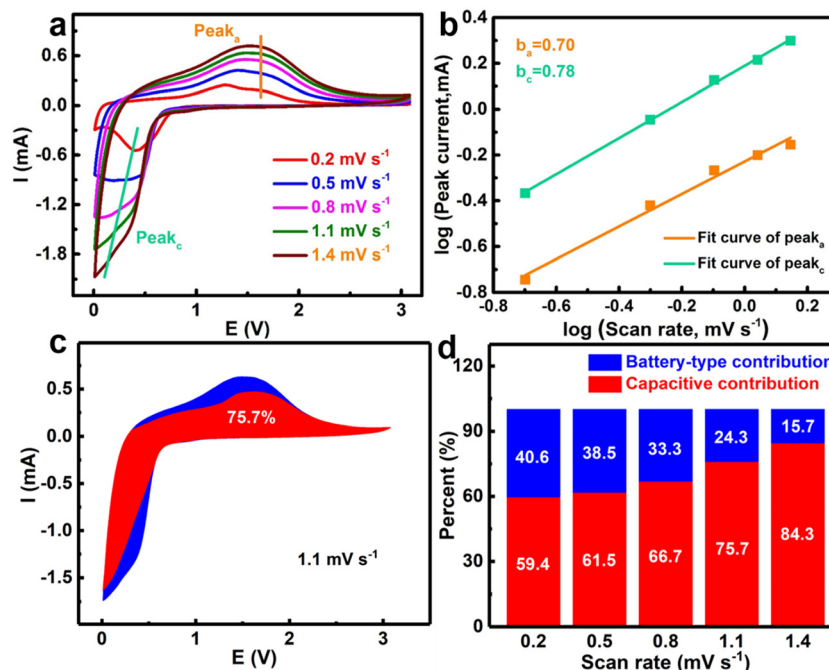
Fig. 6 (a) CV curves of the ZMO-HF electrode at different scan rates, (b) log(i)–log(v) curves (b-value determination), (c) contribution of the surface process (red) at a scan rate of 1.1 mV s^{-1}, and (d) contribution ratios of the surface process (red) at different scan rates of the ZMO-HF electrode.

$$i(V) = k_1 v + k_2 v^{1/2} \tag{3}$$

$$i(V)/v^{1/2} = k_1 v^{1/2} + k_2 v \tag{4}$$

The CV curves of the ZMO-HF electrode material at a scan rate of 1.1 mV s^{-1} are shown in Fig. 6c. The red area represents the pseudocapacitive contribution, and the blue one represents the battery-type contribution, clearly showing the pseudocapacitance-dominated contribution of ~75.7% along with the diffusion-controlled capacity of 24.3%, of the ZMO-HF electrode material at this scan rate. Fig. 6d shows the ratio of the contribution of the pseudocapacitance capacity of 0.2–1.4 mV s^{-1} of the electrode material to the battery. It can be seen intuitively that the contribution of the pseudocapacitance capacity gradually increases with the increase of the scanning speed. The reason for this is probably related to the fact that lithium ions cannot be embedded/removed on time under the higher scanning speeds, which makes lithium ions be stored mainly on and/or near the electrode surface.[45] The pseudocapacitive capacity contributions are estimated as ~59.4%, ~61.5%, ~66.7%, and ~84.3%, respectively, at scanning rates of 0.2, 0.5, 0.8, and 1.4 mV s^{-1}. Therefore, one of the reasons for the excellent electrochemical performance of ZMO-HFs lies in the rapid response characteristic of pseudocapacitive behavior benefiting from their unique hierarchical porous framework.

4. Summary

In summary, ZMO-HFs with single and double shell mixing states were prepared by spray drying. The results show that citric acid monohydrate plays an important role in the surface morphology, structure and structural stability of ZMO-HFs. Furthermore, the emergence of single and double shell hollow microspheres is due to the fact that in the process of droplets being ejected through the nozzle, the unevenness of the nozzle temperature leads to different volatilization rates of liquids in different droplets, so that there are differences in the degree of diffusion of metal ions to the outside. The structure advantage of ZMO-HFs brings excellent electrochemical lithium storage performance. The discharge specific capacity of ZMO-HFs can reach 1043.9 mA h g^{-1} after 160 charge–discharge cycles at a current density of 0.5 A g^{-1}. Even at a current density of 2.0 A g^{-1}, the discharge specific capacity can still be maintained at 724 mA h g^{-1} after 400 cycles of charge and discharge. The excellent electrochemical performance is due to the special structure of the electrode material. The large SSA significantly increases the electroactive sites of the electrode material and improves the ion transport rate. At the same time, the porous hollow structure can effectively alleviate the volume change of the electrode material during the charging and discharging process, and then improve the electrode powder phenomenon caused by stress concentration. It can be concluded that the hollow porous structure not only effectively improves the electrochemical reactivity of ZMO, but also expands its commercial value as an anode for LIBs.

Author contributions

Yamin Zhang: formal analysis, investigation, and writing – original writing – review and editing. Senyang Xu: formal analysis and investigation. Yuyan Wang: formal analysis and investigation. Linrui Hou: validation and funding acquisition. Changzhou Yuan: formal analysis, investigation, conceptualization, writing – review and editing, and funding acquisition.

Conflicts of interest

There are no conflicts to declare.

Acknowledgements

References

1 P. Poizot, S. Laruelle, S. Grugeon, L. Dupont and J. M. Tarascon, Nano-sized transition-metal oxides as negative-electrode materials for lithium-ion batteries, *Nature*, 2000, **407**, 496–499.

2 Z. Li, H. Qin, K. Zhu, P. Liu, X. Chen, X. Wang, H. Li and L. Jiao, Synergistic effect of 3D flexible framework with sodiophilic mesoporous SnO_2 nanosheet arrays on dendrite-free sodium metal batteries, *ACS Appl. Mater. Interfaces*, 2022, **14**, 16394–16403.

3 H. Liu, Y. He, K. Cao, Y. Jiang, X. Liu, Q.-S. Jing and L. Jiao, Activating commercial Al pellets by replacing the passivation layer for high-performance half/full Li-ion batteries, *Chem. Eng. J.*, 2022, **433**, 133572.

4 H. Liu, Y. He, H. Zhang, K. Cao, S. Wang, Y. Jiang, Q.-S. Jing and L. Jiao, Lowering the voltage-hysteresis of CuS anode for Li-ion batteries via constructing heterostructure, *Chem. Eng. J.*, 2021, **425**, 130548.

5 K. Zhong, B. Zhang, S. Luo, W. Wen, H. Li, X. Huang and L. Chen, Investigation on porous MnO microsphere anode for lithium ion batteries, *J. Power Sources*, 2011, **196**, 6802–6808.

6 L. Zhou, H. B. Wu, Z. Wang and X. W. Lou, Interconnected MoO_2 nanocrystals with carbon nanocoating as high-capacity anode materials for lithium-ion batteries, *ACS Appl. Mater. Interfaces*, 2011, **3**, 4853–4857.

7 Y. Sun, X. Hu, W. Luo, F. Xia and Y. Huang, Reconstruction of conformal nanoscale MnO on graphene as a high-capacity and long-life anode material for lithium ion batteries, *Adv. Funct. Mater.*, 2013, **23**, 2436–2444.

8 Q. Hao, J. Wang and C. Xu, Facile preparation of Mn_3O_4 octahedra and their long-term cycle life as an anode material for Li-ion batteries, *J. Mater. Chem. A*, 2014, **2**, 87–93.

9 J. Yue, X. Gu, L. Chen, N. Wang, X. Jiang, H. Xu, J. Yang and Y. Qian, General synthesis of hollow MnO_2, Mn_3O_4 and MnO nanospheres as superior anode materials for lithium ion batteries, *J. Mater. Chem. A*, 2014, **2**, 17421–17426.

10 J. Li, S. Xiong, X. Li and Y. Qian, A facile route to synthesize multiporous $MnCo_2O_4$ and $CoMn_2O_4$ spinel quasi-hollow spheres with improved lithium storage properties, *Nanoscale*, 2013, **5**, 2045–2054.

11 Y. Xiao, J. Zai, L. Tao, B. Li, Q. Han, C. Yu and X. Qian, $MnFe_2O_4$–graphene nanocomposites with enhanced performances as anode materials for Li-ion batteries, *Phys. Chem. Chem. Phys.*, 2013, **15**, 3939–3945.

12 S. Liu, J. Xie, Q. Su, G. Du, S. Zhang, G. Cao, T. Zhu and X. Zhao, Understanding Li-storage mechanism and performance of $MnFe_2O_4$ by in situ TEM observation on its electrochemical process in nano lithium battery, *Nano Energy*, 2014, **8**, 84–94.

13 S. Åsbrink, A. Waśkowska, L. Gerward, J. Staun Olsen and E. Talik, High-pressure phase transition and properties of spinel mathrm $ZnMn_2O_4$, *Phys. Rev. B: Condens. Matter Mater. Phys.*, 1999, **60**, 12651–12656.

14 Y. Yang, Y. Zhao, L. Xiao and L. Zhang, Nanocrystalline $ZnMn_2O_4$ as a novel lithium-storage material, *Electrochem. Commun.*, 2008, **10**, 1117–1120.

15 L. Xiao, Y. Yang, J. Yin, Q. Li and L. Zhang, Low temperature synthesis of flower-like $ZnMn_2O_4$ superstructures with enhanced electrochemical lithium storage, *J. Power Sources*, 2009, **194**, 1089–1093.

16 L. Xiao, Y. Yang, J. Yin, Q. Li and L. Zhang, Low temperature synthesis of flower-like $ZnMn_2O_4$ superstructures with enhanced electrochemical lithium storage, *J. Power Sources*, 2009, **194**, 1089–1093.

17 K. Cai, S.-H. Luo, J. Cong, K. Li, S.-X. Yan, P.-Q. Hou, Y. Song, Q. Wang, Y. Zhang, X. Liu, X. Lei, W. Mu and J. Gao, Sol-gel synthesis of nano block-like $ZnMn_2O_4$ using citric acid complexing agent and electrochemical performance as anode for lithium-ion batteries, *J. Alloys Compd.*, 2022, **909**, 164882.

18 F. Gao, B. Mei, X. Xu, J. Ren, D. Zhao, Z. Zhang, Z. Wang, Y. Wu, X. Liu and Y. Zhang, Rational design of $ZnMn_2O_4$ nanoparticles on carbon nanotubes for high-rate and durable aqueous zinc-ion batteries, *Chem. Eng. J.*, 2022, **448**, 137742.

19 Q. Xia, M. Ni, M. Chen and H. Xia, Low-temperature synthesized self-supported single-crystalline $LiCoO_2$ nanoflake arrays as advanced 3D cathodes for flexible lithium-ion batteries, *J. Mater. Chem. A*, 2019, **7**, 6187–6196.

20 L. Xue, Q. Zhang, X. Zhu, L. Gu, J. Yue, Q. Xia, T. Xing, T. Chen, Y. Yao and H. Xia, 3D $LiCoO_2$ nanosheets assembled nanorod arrays via confined dissolution-recrystallization for advanced aqueous lithium-ion batteries, *Nano Energy*, 2019, **56**, 463–472.

21 J. G. Kim, S. H. Lee, Y. Kim and W. B. Kim, Fabrication of free-standing $ZnMn_2O_4$ mesoscale tubular arrays for lithium-ion anodes with highly reversible lithium storage properties, *ACS Appl. Mater. Interfaces*, 2013, **5**, 11321–11328.

22 G. Zhang, L. Yu, H. B. Wu, H. E. Hoster and X. W. Lou, Formation of $ZnMn_2O_4$ ball-in-ball hollow microspheres as a high-performance anode for lithium-ion batteries, *Adv. Mater.*, 2012, **24**, 4609–4613.

23 P. Zhou, L. Zhong, Z. Liu, M. Liu, T. Zhou, Y. Zhao, X. Lai, J. Bi and D. Gao, Porous $ZnMn_2O_4$ hollow microrods: Facile construction and excellent electrochemical performances for lithium ion batteries, *Appl. Surf. Sci.*, 2022, **578**, 152087.

24 C. Yuan, J. Li, L. Hou, L. Zhang and X. Zhang, Template-free fabrication of mesoporous hollow $ZnMn_2O_4$ sub-microspheres

with enhanced lithium storage capability towards high-performance Li-ion batteries, *Part. Part. Syst. Charact.*, 2014, **31**, 657–663.

25 Y. Deng, S. Tang, Q. Zhang, Z. Shi, L. Zhang, S. Zhan and G. Chen, Controllable synthesis of spinel nano-ZnMn$_2$O$_4$ via a single source precursor route and its high capacity retention as anode material for lithium ion batteries, *J. Mater. Chem.*, 2011, **21**, 11987–11995.

26 M. Yang, C. H. Zhang, N. W. Li, D. Luan, L. Yu and X. W. Lou, Design and synthesis of hollow nanostructures for electrochemical water splitting, *Adv. Sci.*, 2022, **9**, 2105135.

27 H. Yu, Y. Zeng, N. W. Li, D. Luan, L. Yu and X. W. Lou, Confining Sn nanoparticles in interconnected N-doped hollow carbon spheres as hierarchical zincophilic fibers for dendrite-free Zn metal anodes, *Sci. Adv.*, 2022, **8**, eabm5766.

28 Y. Li, S. L. Zhang, W. Cheng, Y. Chen, D. Luan, S. Gao and X. W. Lou, Loading single-Ni atoms on assembled hollow N-rich carbon plates for efficient CO$_2$ electroreduction, *Adv. Mater.*, 2022, **34**, 2105204.

29 T. Zhu, P. Hu, X. Wang, Z. Liu, W. Luo, K. A. Owusu, W. Cao, C. Shi, J. Li, L. Zhou and L. Mai, Realizing three-electron redox reactions in NASICON-structured Na$_3$MnTi(PO$_4$)$_3$ for sodium-ion batteries, *Adv. Energy Mater.*, 2019, **9**, 1803436.

30 X.-F. Chen, L. Qie, L.-L. Zhang, W.-X. Zhang and Y.-H. Huang, Self-templated synthesis of hollow porous submicron ZnMn$_2$O$_4$ sphere as anode for lithium-ion batteries, *J. Alloys Compd.*, 2013, **559**, 5–10.

31 M. Tortosa, F. J. Manjón, M. Mollar and B. Marí, ZnO-based spinels grown by electrodeposition, *J. Phys. Chem. Solids*, 2012, **73**, 1111–1115.

32 H. Li, B. Song, W. J. Wang and X. L. Chen, Facile synthesis, thermal, magnetic, Raman characterizations of spinel structure ZnMn$_2$O$_4$, *Mater. Chem. Phys.*, 2011, **130**, 39–44.

33 L.-X. Zhang, Y.-L. Wang, H.-F. Jiu, H.-Y. Qiu and H.-Y. Wang, Hollow core–shell ZnMn2O4 microspheres as a high-performance anode material for lithium-ion batteries, *Ceram. Interfaces*, 2015, **41**, 9655–9661.

34 X. Su, J. Huang, B. Yan, Z. Hong, S. Li, B. Pang, Y. Luo, L. Feng, M. Zhou and Y. Xia, Hierarchical porous ZnMnO$_3$ yolk–shell microspheres with superior lithium storage properties enabled by a unique one-step conversion mechanism, *RSC Adv.*, 2018, **8**, 31388–31395.

35 H. Chen, L.-X. Ding, K. Xiao, S. Dai, S. Wang and H. Wang, Highly ordered ZnMnO$_3$ nanotube arrays from a

"self-sacrificial" ZnO template as high-performance electrodes for lithium ion batteries, *J. Mater. Chem. A*, 2016, **4**, 16318–16323.

36 Y. Liu, Y. Zhao, Y. Yu, M. Ahmad and H. Sun, Facile synthesis of single-crystal mesoporous CoNiO$_2$ nanosheets assembled flowers as anode materials for lithium-ion batteries, *Electrochim. Acta*, 2014, **132**, 404–409.

37 X.-B. Zhong, Z.-Z. Yang, H.-Y. Wang, L. Lu, B. Jin, M. Zha and Q.-C. Jiang, A novel approach to facilely synthesize mesoporous ZnFe$_2$O$_4$ nanorods for lithium ion batteries, *J. Power Sources*, 2016, **306**, 718–723.

38 X. Guo, X. Lu, X. Fang, Y. Mao, Z. Wang, L. Chen, X. Xu, H. Yang and Y. Liu, Lithium storage in hollow spherical ZnFe$_2$O$_4$ as anode materials for lithium ion batteries, *Electrochem. Commun.*, 2010, **12**, 847–850.

39 W. Dang, F. Wang, Y. Ding, C. Feng and Z. Guo, Synthesis and electrochemical properties of ZnMn$_2$O$_4$ microspheres for lithium-ion battery application, *J. Alloys Compd.*, 2017, **690**, 72–79.

40 Y. Liu, J. Bai, X. Ma, J. Li and S. Xiong, Formation of quasi-mesocrystal ZnMn$_2$O$_4$ twin microspheres via an oriented attachment for lithium-ion batteries, *J. Mater. Chem. A*, 2014, **2**, 14236–14244.

41 Z. Zhao, G. Tian, A. Sarapulova, V. Trouillet, Q. Fu, U. Geckle, H. Ehrenberg and S. Dsoke, Elucidating the energy storage mechanism of ZnMn$_2$O$_4$ as promising anode for Li-ion batteries, *J. Mater. Chem. A*, 2018, **6**, 19381–19392.

42 V. Augustyn, P. Simon and B. Dunn, Pseudocapacitive oxide materials for high-rate electrochemical energy storage, *Energy Environ. Sci.*, 2014, **7**, 1597–1614.

43 K. Zhang, M. Park, L. Zhou, G.-H. Lee, J. Shin, Z. Hu, S.-L. Chou, J. Chen and Y.-M. Kang, Cobalt-doped FeS$_2$ nanospheres with complete solid solubility as a high-performance anode material for sodium-ion batteries, *Angew. Chem., Int. Ed.*, 2016, **55**, 12822–12826.

44 L. Li, J. Zhang, F. Zaman, Y. Y. Wang, Y. M. Zhang, L. R. Hou and C. Z. Yuan, Laser irradiation construction of nanomaterials towards electrochemical energy storage and conversion: ongoing progresses and challenges, *InfoMat*, 2021, **3**, 1393–1421.

45 X. Xu, J. Liu, Z. Liu, J. Shen, R. Hu, J. Liu, L. Ouyang, L. Zhang and M. Zhu, Robust pitaya-structured pyrite as high energy density cathode for high-rate lithium batteries, *ACS Nano*, 2017, **11**, 9033–9040.